crystals

MDPI

Article

Exploring Structural, Optoelectronic, Phonon, Spintronic, and Thermodynamic Properties of Novel Full-Heusler Compounds $TiMCu_2$ (M = Al, Ga, In): Eco-Friendly Materials for Next-Generation Renewable Energy Technologies

Zeesham Abbas [1,*], Amna Parveen [2,*], H. I. Elsaeedy [3], Nejla Mahjoub Said [3] and Mohd Taukeer Khan [4]

[1] Department of Nanotechnology and Advanced Materials Engineering, Sejong University, Seoul 05006, Republic of Korea
[2] College of Pharmacy, Gachon University, No. 191, Hambakmeoro, Yeonsu-gu, Incheon 21936, Republic of Korea
[3] Department of Physics, Faculty of Science, King Khalid University, Abha P.O. Box 9004, Saudi Arabia
[4] Department of Physics, Faculty of Science, Islamic University of Madinah, Al Jamiah, Madinah 42351, Saudi Arabia
* Correspondence: zeeshamabbas035@gmail.com (Z.A.); amnaparvin@gmail.com (A.P.)

Abstract

This work presents a comprehensive first-principles investigation of the structural, electronic, magnetic, optical, and thermodynamic properties of Ti-based full-Heusler compounds $TiMCu_2$ (M = Al, Ga, In). Using density functional theory within the GGA+U framework, the compounds were optimized and analyzed to evaluate their stability and potential for functional applications. The results confirm robust structural and dynamic stability, as verified by elastic constants and phonon dispersion curves. All studied systems exhibit metallic character with pronounced spin polarization, while $TiGaCu_2$ shows the strongest total magnetization, highlighting its suitability for spintronic devices. Optical analyses reveal strong absorption across the visible and near-UV regions, low reflectivity, and favorable dielectric behavior, indicating promise for photovoltaic and optoelectronic applications. Thermodynamic modeling further confirms stability under high temperature and pressure, reinforcing their practical viability. Overall, the $TiMCu_2$ family demonstrates multifunctional characteristics, positioning them as eco-friendly and cost-effective candidates for next-generation renewable energy, spintronic, and optoelectronic technologies.

Keywords: Full-Heusler; first-principles calculations; GGA+U; optical properties; electronic properties; magnetic properties; spintronics

check for updates

Academic Editor: Thomas M. Klapötke

Received: 11 September 2025
Revised: 5 October 2025
Accepted: 6 October 2025
Published: 10 October 2025

Citation: Abbas, Z.; Parveen, A.; Elsaeedy, H.I.; Mahjoub Said, N.; Khan, M.T. Exploring Structural, Optoelectronic, Phonon, Spintronic, and Thermodynamic Properties of Novel Full-Heusler Compounds $TiMCu_2$ (M = Al, Ga, In): Eco-Friendly Materials for Next-Generation Renewable Energy Technologies. *Crystals* **2025**, *15*, 876. https://doi.org/10.3390/cryst15100876

Copyright: © 2025 by the authors. Licensee MDPI, Basel, Switzerland. This article is an open access article distributed under the terms and conditions of the Creative Commons Attribution (CC BY) license (https://creativecommons.org/licenses/by/4.0/).

1. Introduction

Energy conversion materials are essential for satisfying the increasing worldwide demand for energy and reducing energy waste through enhanced recovery material systems [1–4]. In pursuit of a sustainable and eco-friendly alternative to the pollution-intensive and non-biodegradable petroleum-based energy sources, researchers are exploring numerous alternatives [5]. Heusler alloys have garnered attention from the material science community over the past decade because of their wide range of functional features, including shape memory, magnetocaloric, magnetic super elasticity, and barocaloric effects [6–8]. Heusler compounds, which have XYZ and X_2YZ type structures, can be categorized into two categories: half-Heusler and full-Heusler compounds. These ternary compounds are

spin-gapless semiconductors. X and Y represent the transition metals/rare-earth, while Z represents the main-group element. XYZ and X_2YZ possess cubic $C1_b$ and $L2_1$ crystal structure, respectively [1]. The space group $F\bar{4}3m$ (SG # 216) corresponds to half-Heusler compounds, while $Fm\bar{3}m$ (SG # 225) corresponds to full-Heusler compounds. The majority of Heusler alloys were forecasted to be half metallic ferromagnetic materials exhibiting a significant degree of spin polarization. Full-Heusler alloys of the X_2YZ type have recently gained significant interest because of their notable characteristics such as strong spin polarization and huge magnetic moment [9]. According to theoretical studies, Heusler alloys have potential use in spintronic devices [10], thermoelectric devices [11,12], and superconducting devices [13,14]. Heusler alloy compounds are a highly promising category of energy conversion materials that are cost-effective, abundantly available, and include non-poisonous metals [15]. They have the ability to function in both medium temperature ranges (250–650 °C) and high temperature ranges (over 650 °C) [16–18]. Heusler alloys are still being extensively studied for their potential as high-performance thermoelectric (TE) materials in energy conversion processes for TE generators (TEG). Heusler Alloys demonstrates a promising new category of materials for technological applications due to their superior functional properties [19,20]. Numerous materials have been unveiled by researchers with crystalline structures for various technological applications.

Half-metallic (HM) or inter-metallic (IM) materials possess a distinctive characteristic whereby they exhibit semiconductor behavior for one electron spin type and metallic behavior for the other. Crucially, they demonstrate complete spin polarization at the Fermi level [21,22]. Furthermore, due to flat d-bands around Fermi level, Heusler alloys are also potential candidates for thermoelectric device applications. Inter-metallic materials are significant in spintronics as they provide a favorable means of injecting spins into semiconducting substrates, making them highly valuable for a range of technological applications [23,24]. Spintronics is a nascent discipline in electronics that exploits both the electrical charge and the spin characteristic of electrons [25]. The notion of half-metals was initially proposed by Groot et al. in 1983 during their investigation of the electronic structure of NiMnSb, a compound belonging to the half-Heusler family [26]. The research has a revolutionary influence on the advancement of new standard microelectronic devices that include spin-dependent phenomena, such as non-volatile magnetic random-access memory (RAMs) [27] and magnetic sensors [28,29]. Quaternary Heusler alloys exhibiting elevated spin polarization, high Curie temperatures, and reduced Gilbert damping characteristics are more appropriate for spintronic applications and have been extensively investigated both theoretically and experimentally. A significant study has been carried out recently to investigate the characteristics of half-metallic ferromagnetism in different transition metal combinations. Significant instances are NbCoCrAl and NbRhCrAl [30], along with GaP doped with 3d transition metals like V, Cr, and Mn [14]. The subsequent substances have been examined in scholarly research: $Be_{1-x}V_xZ$ (Z = S, Se, or Te, and x = 0.25) [31], $CuMn_2InSe_4$ (a type of spin-gapless semiconductor) [32], Ti_2ZAl (Z = Co, Fe, or Mn) [33], Co_2MnZ (Z = Al, Ge, Si, or Ga) [34], TaCoSn [35], 171 Scandium-based full Heusler compounds [36], ZnCdTMn (T = Fe, Ru, Os, Rh, Ir, Ni, Pd, or Pt) [37], Co_2CrX (X = Al, Ga, or In) [38], and Mn_2ZrX (X = Ge or Si) [39]. Previous research primarily focused on investigating the electronic and magnetic properties of various compounds and alloys, such as Zr_2NiZ (Z = Al, Ga) [40], Zr_2CoAl, Zr_2CoZ (Z = Al, Ga, In, Si, Ge, Sn, Pb, Sb) [41] and Zr_2YZ (Y = Co, Cr, V and Z = Al, Ga, In, Pb, Sn, Tl) with a Li_2AgSb-type structure. Additionally, studies were conducted on Zr_2CoZ (Z = Al, Ga, In, Sn) [42], Zr_2NiZ (Z = Al, Ga) [43], and Zr_2YAl (Y = Cr, Mn, Fe, Co, Ni) [44] to identify potential applications for these materials.

The Full Heusler compounds under investigation exhibit a compelling promise as prospective candidates for researchers in the field of optoelectronic [45] and spintronic devices. Heusler alloys [46] exhibit considerable promise for diverse applications in spintronics, encompassing spin-resonant tunneling diodes, spin light emitting diodes (SLEDs) [47], and spintronic transistors [48]. These materials are essential for their function as spin injectors in various devices that depend on spin-dependent phenomena, such as magnetic random-access memory (MRAM). Inter-metallic Heusler alloys are anticipated to play a significant role in the spintronic industry due to their highly compatible topologies and high Curie temperatures. These alloys are particularly compatible with regularly used binary semiconductors, such as GaAs and GaN, which have zinc-blende crystal structures. The majority of individuals in this family display face-centered cubic (FCC) geometry and XA crystal structures. In this study, we utilized GGA+U-based DFT calculations to examine the influence of Al, Ga and In substitutions on electronic, optical, and spintronic properties of full-Heusler alloys $TiMCu_2$ (M = Al, Ga and In). The main impetus behind these calculations was to investigate the potential of full-Heusler compounds for spintronic and green energy conversion purposes.

2. Materials and Methods

This study includes an examination of the essential properties of pyrochlore oxides using density functional theory (DFT) computations [49–51]. The computations were conducted utilizing the full potential linearized augmented plane wave (FP-LAPW) approach, as implemented in the WIEN2K code. The exchange and correlation potentials are computed using the generalized gradient approximation (GGA) and incorporated the Hubbard potentials (U = 3.0, 5.0 and 7.0 eV). The values of U were selected based on reported values in the literature for various elements [52–54]. The Hubbard potentials (U) are applied to the Ti and Cu-atoms as they contain unfilled d-orbitals [$3d^2$]. This inclusion is deemed essential for effectively investigating correlated electron systems. In the FP-LAPW (Full-Potential Linearized Augmented Plane Wave) method, the unit cell is divided into atomic spheres—known as muffin-tin (MT) spheres—and the interstitial region (IR). Within the interstitial region, the potential is assumed to be approximately constant, whereas inside each muffin-tin sphere, the potential is considered spherically symmetric, depending only on the radial distance R_{MT} ($r \leq R_{MT}$), the muffin-tin radius). Careful selection of appropriate MT radii for different atoms is critical to avoid overlap of atomic spheres and to minimize charge leakage from core orbitals during total energy convergence. Solving the Schrödinger wave equation (SWE) in this framework involves expanding the wavefunction in terms of plane waves in the interstitial region and in terms of spherical harmonics multiplied by radial functions inside the muffin-tin spheres.

$$V(r) = \sum_k V_k e^{i\vec{k}.\vec{r}} \quad (1)$$

In this case, the computation of the spherical potential involves using the Fermi wave vector, denoted by $\vec{k}$, and the magnitude of the plane wave, denoted by V_k.

$$V(r) = \sum_{l,m} V_{lm}(r) Y_{lm}(r) \quad (2)$$

The wave functions were expanded by setting the maximum angular momentum quantum number $l_{max} = 10$ within the muffin-tin (MT) radii. A cutoff energy of -6.0 Ry was applied, with energy and force convergence criteria of 10^{-3} Ry/au and 10^{-4} Ry, respectively. The plane-wave thresholds within the irreducible Brillouin zone (IBZ) were set as $R_{MT} \times K_{max} = 7.0$ and $G_{max} = 12$. Calculations employed a dense $12 \times 12 \times 12$ k-point

mesh, totaling 500 k-points. Here, R_{MT} represents the minimum muffin-tin radius, and K_{max} denotes the maximum reciprocal lattice vector. Geometry relaxation was achieved by reducing the forces on each atom to less than 10^{-3} Ry/au. The optimized crystalline structures of $TiMCu_2$ (M = Al, Ga, In) are shown in Figure 1, and the corresponding Wyckoff positions are listed in Table 1.

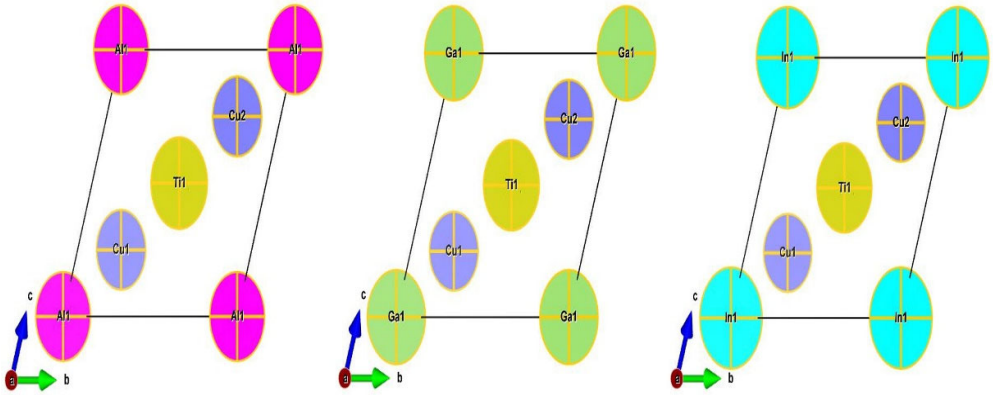


Figure 1. The visual representation of the crystalline unit cells for $TiMCu_2$ (M = Al, Ga and In).

Table 1. Wycoff positions for $TiMCu_2$ (M = Al, Ga and In).

Compound	Element	Wycoff	x	y	z
$TiAlCu_2$	Ti	4a	0	0	0
	Al	4b	0	1/2	0
	Cu	8c	3/4	1/4	3/4
$TiGaCu_2$	Ti	4a	0	0	0
	Ga	4b	0	1/2	0
	Cu	8c	3/4	1/4	3/4
$TiInCu_2$	Ti	4a	0	0	0
	In	4b	0	1/2	0
	Cu	8c	3/4	1/4	3/4

3. Results

3.1. Structural Properties

In this section of the manuscript, the structural stability of $TiMCu_2$ (M = Al, Ga and In) is examined. This was accomplished by figuring out each of their unique structural characteristics. The bulk modulus, ground state energy, pressure derivative of bulk modulus, and optimum volume symbolized by B, E_0, B^P, and V_0 are crucial factors to take into account while examining the structural stability of the materials being studied. These Ti-based full-Heusler's basic properties have been evaluated by calculating their total energy in relation to their ideal volume. By using the equation of state (EOS) formulated by Birch-Murnaghan, $TiMCu_2$ (M = Al, Ga and In) was structurally optimized [55].

$$E_{tot}(V) = E_0(V) + \frac{B_0 V}{B'(B'-1)}\left[B\left(1-\frac{V_0}{V}\right) + \left(\frac{V_0}{V}\right)^{B'} - 1\right] \quad (3)$$

Figure 2 presents the calculated structural optimization (E–V) curves for $TiMCu_2$ (M = Al, Ga, In). The minimum of each curve corresponds to the equilibrium volume, with the associated energy representing the ground-state energy. The optimized lattice parameters, obtained through volume optimization, reflect the equilibrium configuration of the material's crystalline structure. To confirm the reliability of our structural model, we compared the total energies of the conventional $L2_1$ (Fm-3m, SG #225) and inverse XA

(F–43m, SG #216) configurations of $TiMCu_2$ (M = Al, Ga, In) using identical computational settings within the GGA+U framework. The results clearly indicate that the XA configuration possesses lower total energy than the $L2_1$ phase for all studied compounds, confirming it as the thermodynamically stable ground-state structure. The calculated energy differences ($\Delta E = E_{L2_1} - E_{XA}$) range between 0.26–0.45 eV per formula unit, favoring the XA arrangement. This stability trend is consistent with earlier first-principles investigations on Ti- and Zr-based Heusler alloys. The verification of the XA ground-state ensures that all subsequent evaluations—electronic, magnetic, optical, and thermodynamic—are based on the energetically favored configuration, thereby providing a robust and physically justified foundation for the reported properties. The computed values of these optimized structural parameters are summarized in Table 2. Ideally, such materials should demonstrate high electrical conductivity, significant mechanical strength, and the ability to sustain large bulk modulus values.

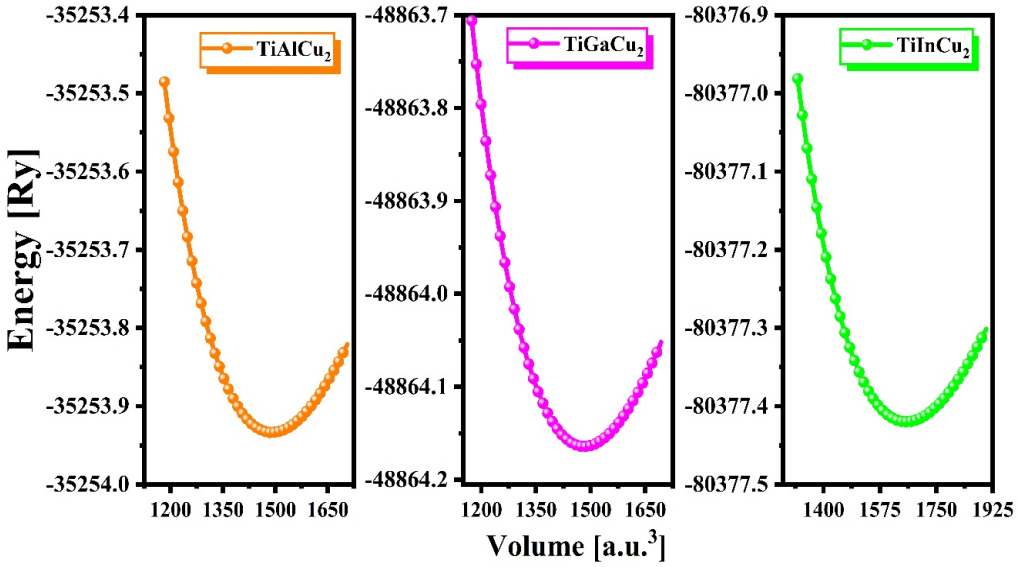


Figure 2. The visual representation of the structural optimization [E-V] spectra for $TiMCu_2$ (M = Al, Ga and In).

Table 2. Tabulated ground state parameters for $TiMCu_2$ (M = Al, Ga and In).

Compounds	a (Å)	V (Å^3)	B (GPa)	B^P (GPa)	E_0 (XA) (Ry)	E_0 ($L2_1$) (Ry)	E_g (eV)
$TiAlCu_2$	6.04	1490.02	135.09	4.57	−35,253.93	−35,253.67	Metallic
$TiGaCu_2$	6.03	1482.05	138.23	4.36	−48,864.16	−48,863.71	
$TiInCu_2$	6.26	1656.44	121.78	4.75	−80,377.42	−80,377.15	

3.2. Electronic Properties

All figures and tables are cited in the main text as Figure 1, Table 1, etc. This section presents a detailed analysis of the computed electronic properties, including the density of states (DOS) and energy band dispersions, for $TiMCu_2$ (M = Al, Ga, In). The primary electronic transitions between the valence and conduction bands are interpreted based on the electronic characteristics of these compounds. The calculated energy band structures are plotted along high-symmetry points (R → Γ → X → M → Γ) in the first Brillouin zone over an energy range of −5.0 to 5.0 eV, with the Fermi level (E_F) set at 0 eV. Similarly, the DOS spectra are shown over −6.0 to 6.0 eV, also with E_F positioned at 0 eV.

3.2.1. Energy Band Structures

The energy band structures of $TiMCu_2$ (M = Al, Ga, In) are presented in Figure 3(i–iv (a–c)), calculated using spin-polarized GGA and GGA+U methods with U values of 3.0, 5.0, and 7.0 eV. The Fermi energy level (E_F) is defined as the energy corresponding to zero in the band structure. The metallic character of $TiMCu_2$ (M = Al, Ga, In) is confirmed by the GGA+U calculations. In both GGA and GGA+U approximations, the metallic behavior arises from the crossing of energy bands at the Fermi level, as illustrated in Figure 3(i–iv (a–c)) for both spin channels. The band gap (E_g) is determined by the energy difference between the conduction band minimum (CBM) and the valence band maximum (VBM). Our calculations indicate an overlap between the valence and conduction bands, leading to the metallic nature of these compounds. These compounds demonstrate notable dispersion in k-space, particularly at certain sites, which verifies the increased mobility of electron–hole carriers in the conduction band (CB) and valence band (VB). Although some full-Heusler alloys exhibit half-metallicity, our $TiMCu_2$ (M = Al, Ga and In) compounds do not satisfy the Slater-Pauling electron count and show strong Ti-Cu d-d hybridization. Spin-resolved DOS calculations reveal both spin channels crossing the Fermi level and only a small exchange splitting. These features intrinsically yield metallic behavior in both spins, consistent with our DFT results and with reports on other Ti-based Heuslers.

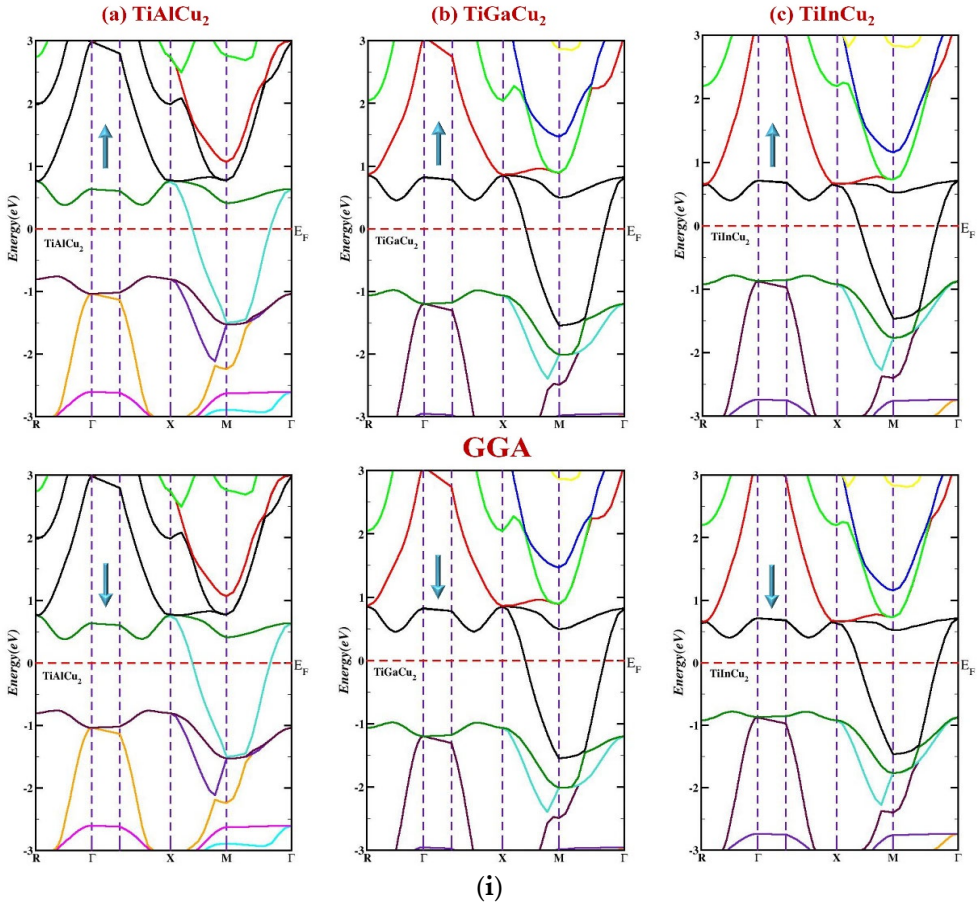


Figure 3. *Cont.*

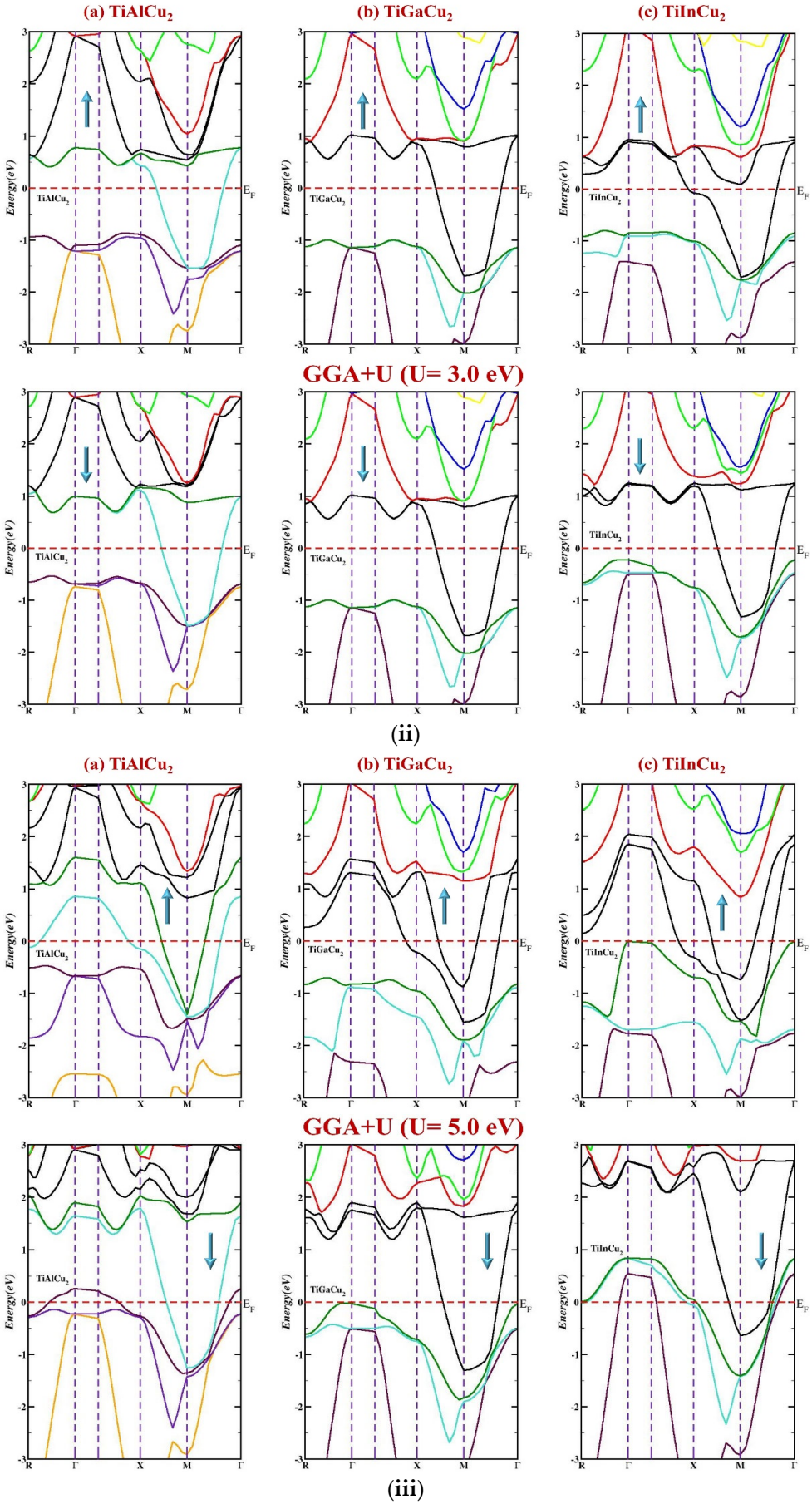


Figure 3. *Cont*.

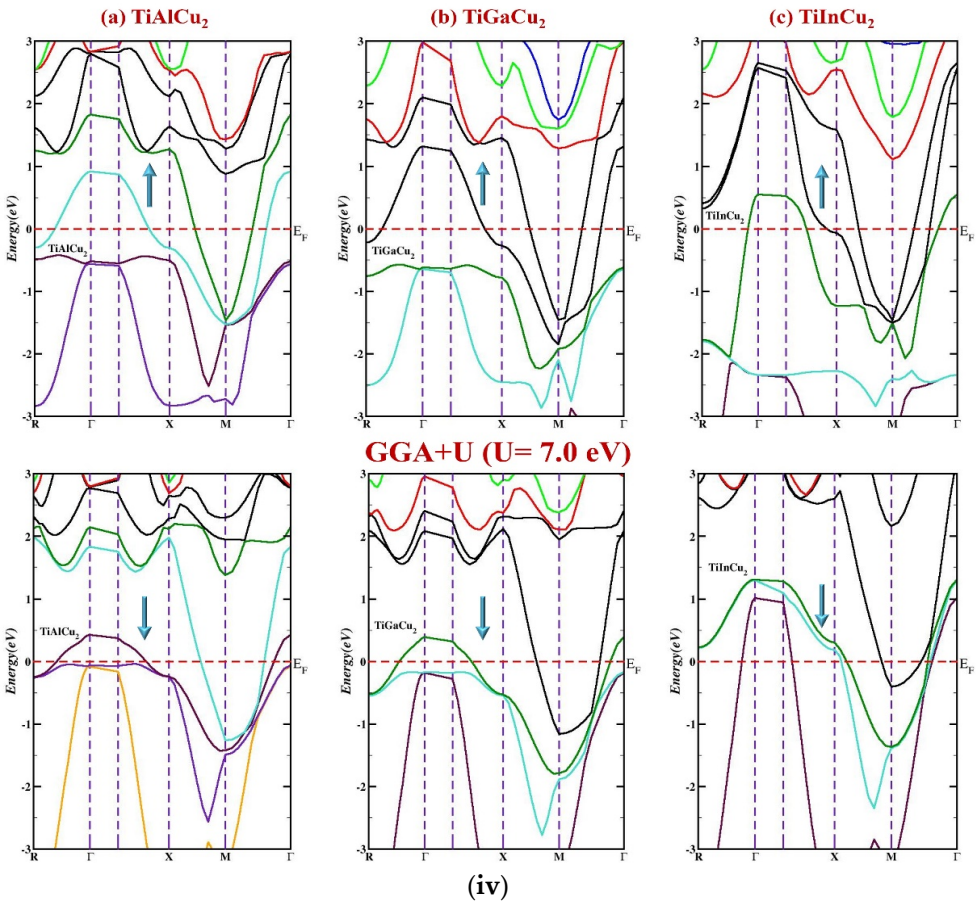


Figure 3. The visual representation of the calculated energy band structures for $TiMCu_2$ (M = Al, Ga, In) using (**i**) GGA, and GGA+U (**ii**) U = 3.0 eV, (**iii**) U = 5.0 eV, and (**iv**) U = 7.0 eV.

A comparison of the energy band gaps, and magnetic moments has been made in Table 2.

3.2.2. Density of States

In order to comprehend the electronic properties of $TiMCu_2$ (M = Al, Ga, In), we have calculated the spin-polarized total density of states (TDOS) and partial density of states (PDOS) as a function of energy. The TDOS for $TiMCu_2$ (M = Al, Ga, In) is illustrated in Figure 4 employing GGA and GGA+U (U = 3.0, 5.0, and 7.0 eV) methodology. The PDOS, spintronic, and optical properties are provided just for GGA+U (U = 5.0 eV). The results indicate that the total density of states (TDOS) spectra for $TiAlCu_2$ and $TiGaCu_2$ exhibit similar TDOS, whereas $TiInCu_2$ displays distinct spectra. This is noteworthy considering that all compounds share the same crystal structure, with the only difference being the substitution of Al with Ga and In atoms. It is evident from the computed spectra of $TiMCu_2$ (M = Al, Ga, In) that all compounds exhibit comparable characteristics in the valence band. Variations in the TDOS profiles in spin ↑ and spin ↓ states validate the presence of magnetic moments in these full-Heusler compounds. The following expression can be employed to investigate spin-polarization (P) exhibited by $TiMCu_2$ (M = Al, Ga, In).

$$P = \frac{N\uparrow(E_F) - N\downarrow(E_F)}{N\uparrow(E_F) + N\downarrow(E_F)} \tag{4}$$

where $N\uparrow(E_F)$ and $N\downarrow(E_F)$ are used to denote density of states at Fermi level for spin ↑ and spin ↓ states, respectively. The values of P calculated for $TiMCu_2$ (M = Al, Ga, In) are

shown in Table 3. The magnetic moments in $TiMCu_2$ (M = Al, Ga, In) originate from the differences in the stature and configurations of the TDOS spectra illustrated in Figure 4.

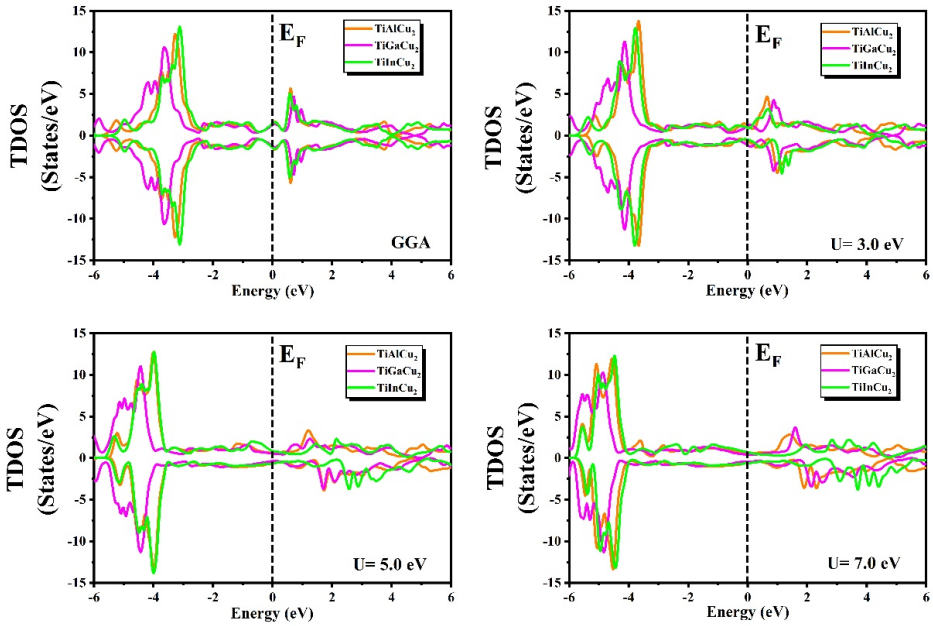


Figure 4. The visual representation of the total density of states (TDOS) for $TiMCu_2$ (M = Al, Ga, In) calculated using GGA and GGA+U (U = 3.0, 5.0 and 7.0 eV) approximations.

Table 3. Tabulated values of spin-polarization (%) for $TiMCu_2$ (M = Al, Ga and In) at various values of U.

Compounds	GGA	GGA+U		
		3.0	5.0	7.0
$TiAlCu_2$	0.035	28.42	1.08	5.70
$TiGaCu_2$	0.009	0.067	22.31	0.014
$TiInCu_2$	0.016	33.69	13.89	7.63

Figure 5 displays the partial density of states (PDOS) solely for $TiAlCu_2$, which was computed using the GGA+U approximation. The E_g is universally set to 0.0 eV for all substances. The purpose of calculating PDOS is to obtain information about the relative contributions of various atomic states to the conduction and valence bands at the Fermi level (E_F). Figure 5 clearly demonstrates that Cu-atoms provide considerable contributions to the valence band. Furthermore, there are also modest contributions from Ti-atoms in the VB for both spin states. The CB predominantly comprises Ti-atoms in both spin states. In addition, there are minor contributions from Al and Cu-atoms in the CB. By examining Figure 5, it is evident that the Cu [$3d^{10}$] orbital makes substantial contributions to the VB. On the other hand, the VB also exhibits small contributions from Ti [$3d^2$] and Al [$3p^1$] orbitals. Figure 5 displays notable contributions from Ti [$3d^2$] orbitals in the CB, together with slight contributions from the Cu [$3d^{10}$], Al [$3s^2$] and Al [$3p^1$] orbital. The obtained PDOS graphs for $TiAlCu_2$ indicate that the most likely electronic transitions among valence and conduction bands occur between the Cu [$3d^{10}$], Ti [$3d^2$] and Al [$3p^1$] orbitals and the Ti [$3d^2$] and Al [$3p^1$] orbitals.

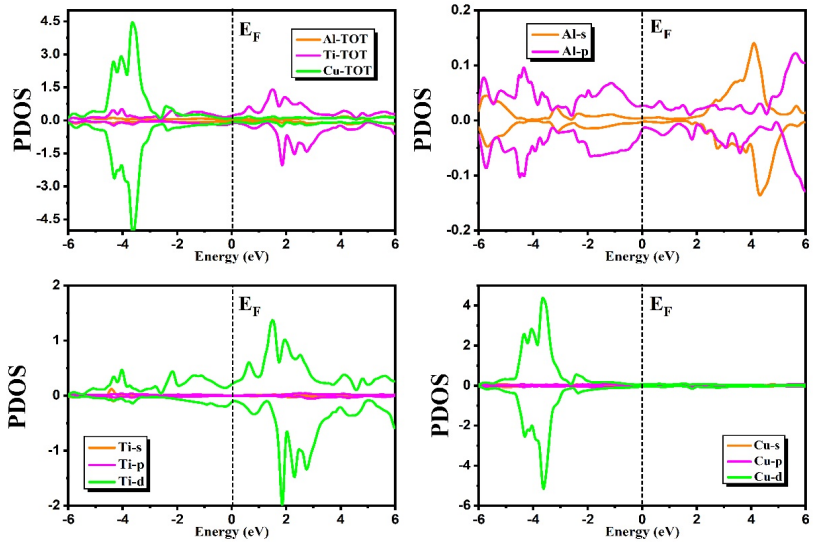


Figure 5. The visual representation of the partial density of states (PDOS) for $TiAlCu_2$.

Figure 6 displays the partial density of states (PDOS) solely for $TiGaCu_2$, which was computed using the GGA+U approximation. The E_g is universally set to 0.0 eV for all substances. The purpose of calculating PDOS is to obtain information about the relative contributions of various atomic states to the conduction and valence bands at the Fermi level (E_F). Figure 6 clearly demonstrates that Cu-atoms provide considerable contributions to the VB. Furthermore, there are also modest contributions from Ti-atoms in the valence band for both spin states. The conduction band predominantly comprises Ti-atoms in both spin states. In addition, there are slight contributions from Ga and Cu-atoms in the CB. By examining Figure 6, it is evident that the Cu [$3d^{10}$] orbital makes substantial contributions to the VB. On the other hand, the VB also exhibits small contributions from Ti [$3d^2$] and Ga [$4p^1$] orbitals. Figure 6 displays notable contributions from Ti [$3d^2$] orbitals in the CB, together with slight contributions from the Cu [$3d^{10}$], Ga [$4s^2$] and Ga [$4p^1$] orbital. The obtained PDOS graphs for $TiGaCu_2$ indicate that the most likely electronic transitions among valence and conduction bands occur between the Cu [$3d^{10}$], Ti [$3d^2$] and Ga [$4p^1$] orbitals and the Ti [$3d^2$] and Ga [$4p^1$] orbitals.

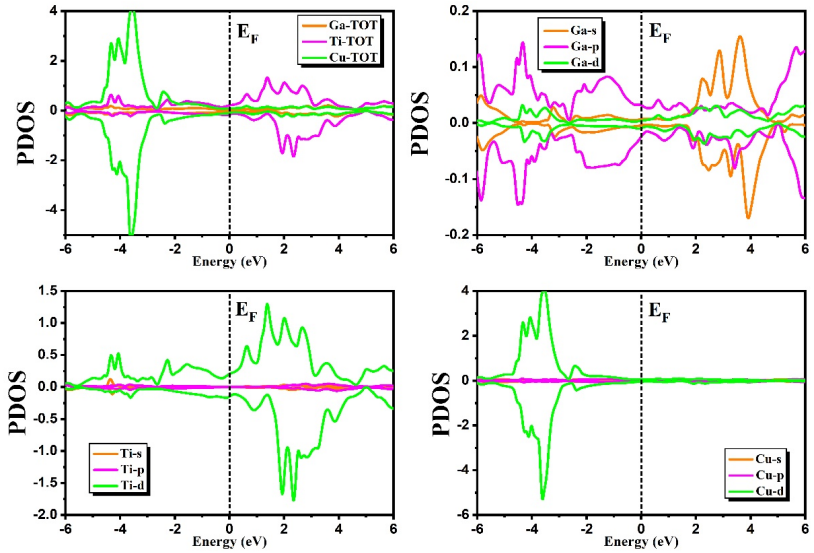


Figure 6. The visual representation of the partial density of states (PDOS) for $TiGaCu_2$.

Figure 7 displays the partial density of states (PDOS) solely for $TiInCu_2$, which was computed using the GGA+U approximation. The E_g is universally set to 0.0 eV for all substances. The purpose of calculating PDOS is to obtain information about the relative contributions of various atomic states to the conduction and valence bands at the Fermi level (E_F). Figure 7 clearly demonstrates that Cu-atoms provide considerable contributions to VB. Furthermore, there are also modest contributions from Ti-atoms in the valence band for both spin states. The CB predominantly comprises Ti-atoms in both spin states. In addition, there are slight contributions from In and Cu-atoms in the CB. By examining Figure 7, it is evident that the Cu [$3d^{10}$] orbital makes substantial contributions to the VB. On the other hand, the VB also exhibits small contributions from Ti [$3d^2$] and In [$5p^1$] states. Figure 7 displays notable contributions from Ti [$3d^2$] states in the CB, together with slight contributions from the Cu [$3d^{10}$], In [$5s^2$] and In [$4d^{10}$] orbital. The obtained PDOS graphs for $TiInCu_2$ indicate that the most likely electronic transitions among valence and conduction bands occur between the Cu [$3d^{10}$], Ti [$3d^2$] and In [$5p^1$] orbitals and the Ti [$3d^2$] and In [$5s^2$] orbitals.

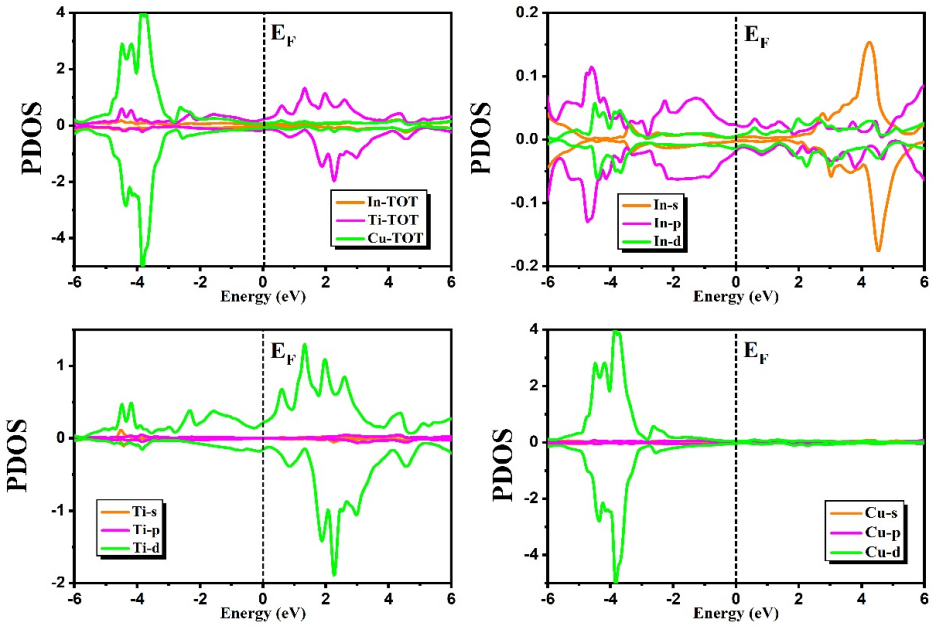


Figure 7. The visual representation of the partial density of states (PDOS) for $TiInCu_2$.

3.3. Fermi Surface

The Fermi surfaces (FS) of the ferromagnetic compounds $TiMCu_2$ (M = Al, Ga, In) were analyzed to gain a detailed understanding of their electronic structures by examining the accessible electronic states for both spin channels. High-symmetry points within the first Brillouin zone were selected to investigate the arrangement of energy bands near the Fermi level. The FS for $TiMCu_2$ (M = Al, Ga, In) are presented in Figure 8a–c. Electrons at the Fermi level play a critical role in determining the electrical conductivity of these compounds. The metallic character of $TiMCu_2$ (M = Al, Ga, In) is corroborated through analysis of the energy band dispersions, density of states (DOS), and Fermi surface plots. Fermi surface calculations provide insight into the electronic states beyond the Fermi level. The FS of $TiMCu_2$ (M = Al, Ga, In) displays distinct electronic sheets and hole pockets, with electrons and holes identified by colored and uncolored regions, respectively. Moreover, the FS analysis elucidates the contribution of electrons to the material's electronic properties. Notably, metallic behavior is observed in both spin channels of the studied compounds.

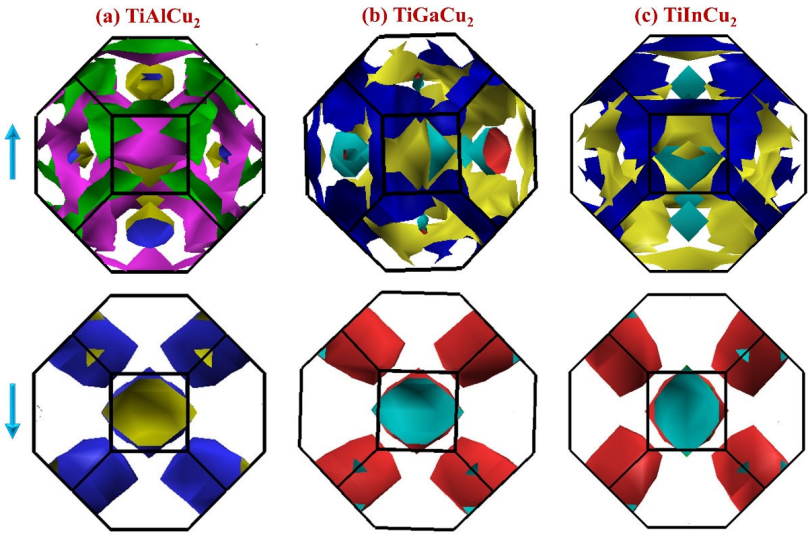


Figure 8. The visual representation of the Fermi surface (FS) for $TiMCu_2$ (M = Al, Ga, In).

The Fermi surface configuration is strongly related to the transport properties and electrical conductivity of $TiMCu_2$ (M = Al, Ga, In). The FS iso-surfaces reveal significant variations in conductivity among these compounds. Additionally, different colors on the Fermi surface represent the varying velocities of the electrons contributing to it. Fast-moving electrons are allocated the colors red and violet, while electrons with mild and intermediate velocity are assigned various hues. It is important to mention that $TiAlCu_2$ demonstrates the highest level of electronic conductivity compared to $TiGaCu_2$ and $TiInCu_2$.

3.4. Phonon Dispersions

It is essential to account for phonon dispersion to fully comprehend the evolving conditions, thermodynamic properties, and vibrational analysis by Raman spectroscopy in crystalline materials [56]. The phonon frequencies of the layers were determined using the Perdew–Burke–Ernzerhof (PBE) functional within the framework of Density Functional Perturbation Theory (DFPT). Figure 9 presents the calculated phonon spectra for $TiMCu_2$ (M = Al, Ga, In). The phonon dispersion curves were evaluated along the high-symmetry directions of the first Brillouin zone (R–Γ–X–M–Γ). According to vibrational theory, a material is dynamically stable if its phonon spectrum contains no imaginary frequencies; the presence of any imaginary modes indicates dynamic instability. Analysis of $TiMCu_2$ (M = Al, Ga, In) confirms its dynamic stability, as no imaginary frequencies are observed in the spectra.

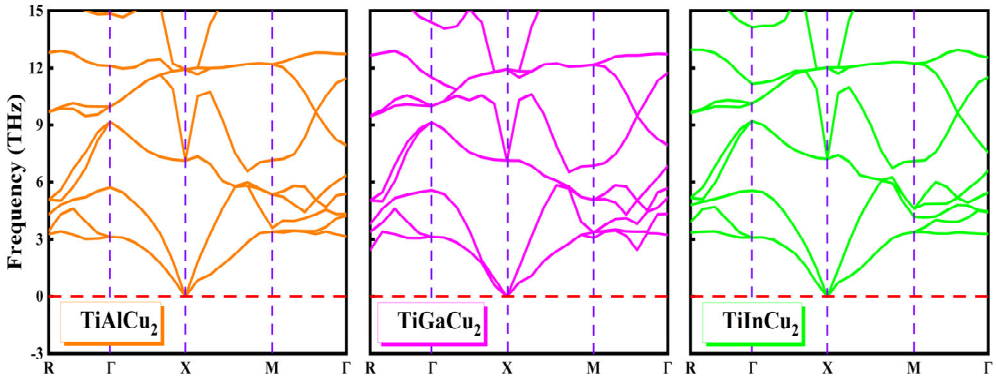


Figure 9. The visual representation of the phonon dispersions for $TiMCu_2$ (M = Al, Ga, In).

3.5. Magnetic Properties

This section of the manuscript presents and discusses the obtained magnetic moments for $TiMCu_2$ (M = Al, Ga, In). A fundamental property for magnetic materials is magnetic anisotropy for spintronic applications. The existence of magnetic moments in different materials is ascribed to the hybridization of 3d electrons in conjunction with other electrons [57]. High values of tunnel magnetoresistance (TMR) are required for an efficient magnetic tunnel junction (MTJ). The Galanakis model states that the difference observed between the spin up and spin down channels in the occupied bands of half-Heusler compounds corresponds to the spin magnetic moment [58]. The magnetic moments for $TiMCu_2$ (M = Al, Ga, In) are listed in Table 4, including both the total and partial values. Table 1 illustrates that M-atoms (M = Al, Ga, In) provide a substantial contribution to the overall magnetization of $TiMCu_2$ (M = Al, Ga, In). $TiGaCu_2$ demonstrates the highest magnitude of total magnetization. The presence of a negative sign in m_{Ti} and m_{Cu} signifies that these atoms possess magnetic moments that are oriented in the opposite direction as m_M in these compounds. The Hubbard Hamiltonian (U) corrected GGA calculations reveal a significant splitting of the localized orbitals in these compounds, resulting in diverse magnetic interactions. The strong magnetic couplings observed in metallic compounds (Al, Ga, In) elements can be attributed to the hybridization of localized states, which are found in these elements. Consequently, they exhibit a diverse array of magnetic properties. The magnetic moments of $TiMCu_2$ (M = Al, Ga, In) were determined using GGA+U-based spin-polarized simulations. The band structures of the investigated compounds demonstrate their metallic character.

Table 4. Tabulated total and partial magnetic moments (μ_B) of $TiMCu_2$ (M = Al, Ga, In).

Compounds	Method	Magnetic Moment (μ_B)				
		m_{int}	m_{Ti}	m_M	m_{Cu}	m_{tot}
$TiAlCu_2$	GGA	−0.0001	−0.0006	0.00002	0.0001	−0.0007
	GGA+U	0.0283	−0.0222	0.6982	−0.0449	0.6594
$TiGaCu_2$	GGA	0.00000	−0.00007	0.0000	0.00001	−0.00006
	GGA+U	0.0545	−0.0222	0.7546	−0.0313	0.7556
$TiInCu_2$	GGA	−0.00002	−0.00006	0.0000	0.0000	−0.00008
	GGA+U	0.0555	−0.0173	0.7354	−0.0283	0.7452

3.6. Optical Properties

In order to investigate the behavioral characteristics of optics in $TiMCu_2$ (M = Al, Ga, In), the following material properties are calculated and determined through electronic resilience: reflectance, index of refraction, absorption coefficient, energy loss function, and relative permittivity. Wave motion is the underlying cause of all these phenomena. The evaluation of the possible applications of full-Heusler materials $TiMCu_2$ (M = Al, Ga, In) in photovoltaic systems necessitates the examination of their optical characteristics via electronic band structures. A thorough understanding of variations in optical properties can be gained by examining the material's response to different photon energies ($E = h\nu$) [59]. This investigation deepens insight into the frequency dependence of these parameters by leveraging the material's inherent optical characteristics. At a fundamental level, the optical behavior of crystalline solids is described by the frequency-dependent dielectric function $\varepsilon(\omega)$, which measures the degree of polarization induced by electromagnetic radiation. The dielectric function $\varepsilon(\omega)$ is determined using the following equation:

$$\varepsilon(\omega) = \varepsilon_1(\omega) + i\varepsilon_2(\omega) \quad (5)$$

In the complex dielectric function $\varepsilon(\omega)$, the imaginary part $\varepsilon_2(\omega)$ represents the absorptive component, while the real part $\varepsilon_1(\omega)$ corresponds to the dispersive component. Variations in the electronic band structure directly influence the behavior of $\varepsilon(\omega)$. The dispersion of incident photons is derived from the real component $\varepsilon_1(\omega)$, whereas their absorption is described by the imaginary component $\varepsilon_2(\omega)$. The value of $\varepsilon_2(\omega)$ can be calculated using the following equation:

$$\varepsilon_2(\omega) = \frac{8\pi^2 e^2}{\omega^2 m^2} \sum_n \sum_{n'} \int \left|P^v_{nn'}(k)\right|^2 f_{kn}(1 - f_{nn'}) \delta(E^k_n - E^k_{n'} - \omega) \frac{d^3k}{(2\pi)^3} \quad (6)$$

To compute values of $\varepsilon_2(\omega)$ in this scenario, you will want the electronic charge (e), mass of the electron (m), and energy of one electron ($E^k_n(k)$). Additionally, we need the Fermi–Dirac function (f_{kn}) and the matrix components of momentum dipole projection ($P^k_{nn'}(k)$). The obtained values of $\varepsilon_2(\omega)$ are mostly used to evaluate the electronic properties of crystalline solids. The phenomena of incoming photon absorption are intricately connected to the parameter $\varepsilon_2(\omega)$. The $\varepsilon_2(\omega)$ spectra for $TiMCu_2$ (M = Al, Ga, In) were determined and are displayed in Figure 10, covering an energy range from 0 to 14.0 eV. The $\varepsilon_2(\omega)$ spectra exhibit prominent peaks resulting from electronic transitions between the populated valence band (VB) and the empty conduction band (CB). At first, it is seen that there are no noticeable peaks in the spectra of $\varepsilon_2(\omega)$. Following that, the peaks corresponding to $TiMCu_2$ (M = Al, Ga, In) appear at around 0.0 eV. The $\varepsilon_2(\omega)$ spectra display distinct peaks originating from electronic transitions between the filled valence band (VB) and the empty conduction band (CB). Initially, no significant peaks are observed; subsequently, peaks for $TiMCu_2$ (M = Al, Ga, In) emerge near 0.0 eV. This value corresponds to the threshold value of $\varepsilon_2(\omega)$. The results presented in Figure 10 clearly demonstrate that significant absorption peaks are present in the near UV range. The distinct peaks in the $\varepsilon_2(\omega)$ spectra of $TiMCu_2$ (M = Al, Ga, In) are exhibited in visible region at energies around 2.0 eV. The energy levels corresponding to the distinct peaks are tabulated in Table 5. Therefore, these full-Heusler compounds show strong potential as viable materials for solar cells and other optoelectronic applications operating in the visible and near-UV ranges.

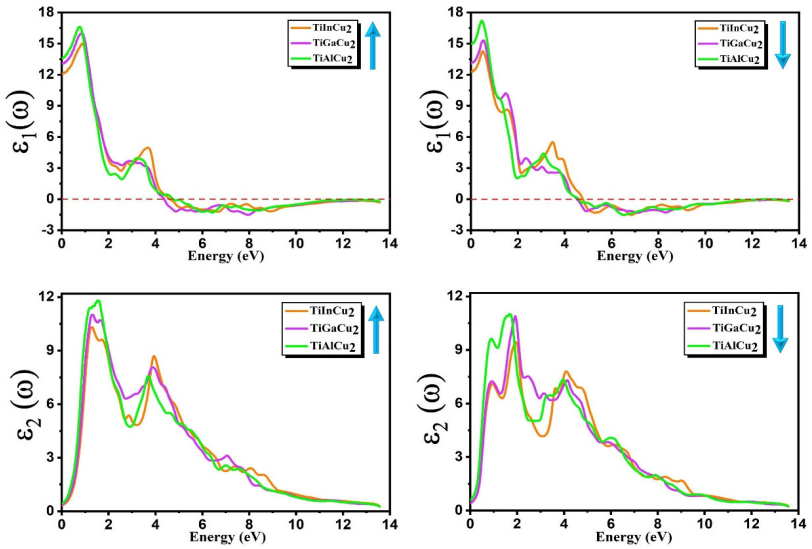


Figure 10. The visual representation of the real part $\varepsilon_1(\omega)$ and imaginary part $\varepsilon_2(\omega)$ of complex dielectric function for $TiMCu_2$ (M = Al, Ga, In).

Table 5. Tabulated values of energies (eV) corresponding to distinct peaks of $\varepsilon_2(\omega)$, $K(\omega)$, $L(\omega)$, $\sigma(\omega)$ and $I(\omega)$ for $TiMCu_2$ (M = Al, Ga, In).

Compounds	$\varepsilon_2(\omega)$		$K(\omega)$		$L(\omega)$		$\sigma(\omega)$		$I(\omega)$	
	↑	↓	↑	↓	↑	↓	↑	↓	↑	↓
$TiAlCu_2$	1.58	1.63	1.67	1.78	13.37	13.52	3.64	3.97	8.34	6.43
$TiGaCu_2$	1.33	1.91	4.12	1.97	13.40	13.58	3.91	4.17	7.90	8.31
$TiInCu_2$	1.27	1.97	4.46	4.95	13.15	13.32	3.96	4.70	8.84	9.19

The real component $\varepsilon_1(\omega)$ can be ascertained by utilizing the Kramers–Kronig relation and the estimated values of $\varepsilon_2(\omega)$:

$$\varepsilon_1(\omega) = 1 + \frac{2}{\pi} P \int_0^{\infty} \frac{\omega' \varepsilon_2(\omega')}{\omega'^2 - \omega^2} d\omega' \tag{7}$$

The dielectric tensor values are eventually employed to deduce the optical properties of full-Heusler compounds $TiMCu_2$ (M = Al, Ga, In) based on their electronic band structures. The $\varepsilon_1(\omega)$ spectra for $TiMCu_2$ (M = Al, Ga, In) were computed and are displayed in Figure 10, covering an energy range from 0 to 14.0 eV. The static values, also known as the zero-frequency limit, refer to the values of $\varepsilon_1(\omega)$ that are seen at the y-axis when ω is equal to zero. The equation proposed by Penn can be used to establish a relationship between the energy bandgap (E_g) and $\varepsilon_1(0)$:

$$\varepsilon_1(0) \approx 1 + \left(\frac{\hbar\omega_p}{E_g}\right)^2 \tag{8}$$

Based on the results depicted in Figure 10, the initial values of $\varepsilon_1(0)$ for $TiMCu_2$ (M = Al, Ga, In) are tabulated in Table 6. The highest degree of scattering of incoming photons in the full-Heusler compounds takes place around 1.0 eV. Figure 10 displays a mostly similar pattern of $\varepsilon_1(\omega)$ for $TiMCu_2$ (M = Al, Ga, In), with minimal differences detected in the magnitude and location of the peaks. The graphs of $\varepsilon_1(\omega)$ cross the y-axis ($y = 0$) at approximately 4.78, 4.41, and 4.62 eV for $TiAlCu_2$, $TiGaCu_2$, and $TiInCu_2$, respectively, in spin ↑ channel. The plasmon frequency in spin ↓ channel for $TiAlCu_2$, $TiGaCu_2$, and $TiInCu_2$ are 4.70, 4.61, and 4.81 eV, respectively. This point is identified as the plasmon frequency, at which the compounds exhibit metallic behavior in the negative region and achieve nearly 100% photon reflectivity across a broad spectrum of incident wavelengths.

Table 6. Tabulated static values of $\varepsilon_1(\omega)$, $n(\omega)$, $R(\omega)$ for $TiMCu_2$ (M = Al, Ga, In).

Compounds	$\varepsilon_1(0)$		$n(0)$		$R(0)$	
	↑	↓	↑	↓	↑	↓
$TiAlCu_2$	13.6	15.0	3.69	3.87	0.33	0.35
$TiGaCu_2$	13.1	13.1	3.61	3.62	0.32	0.32
$TiInCu_2$	12.1	12.3	3.48	3.50	0.31	0.31

The refractive index $n(\omega)$ represents the ratio of the speed of light in vacuum to its speed within a given medium. It is a key parameter for analyzing light–matter interactions and photon dispersion. Using the specified equation, $n(\omega)$ can be determined from the calculated values of the real and imaginary parts of the dielectric function, $\varepsilon_1(\omega)$ and $\varepsilon_2(\omega)$.

$$n(\omega) = \left\{ \frac{\varepsilon_1(\omega)}{2} + \frac{\sqrt{\varepsilon_1^2(\omega) + \varepsilon_2^2(\omega)}}{2} \right\}^{\frac{1}{2}} \tag{9}$$

The $n(\omega)$ spectra of $TiMCu_2$ (M = Al, Ga, In), calculated over the 0–14.0 eV energy range, are presented in Figure 11. The refractive index $n(\omega)$, analogous to the real part of the dielectric function $\varepsilon_1(\omega)$, also illustrates photon dispersion. The static or zero-frequency value corresponds to $n(\omega)$ at $\omega = 0$, represented by the interception on the y-axis. The relationship between the initial values $n(0)$ and $\varepsilon_1(0)$ can be expressed using the following equation:

$$n(0) = \sqrt{\varepsilon_1(0)} \tag{10}$$

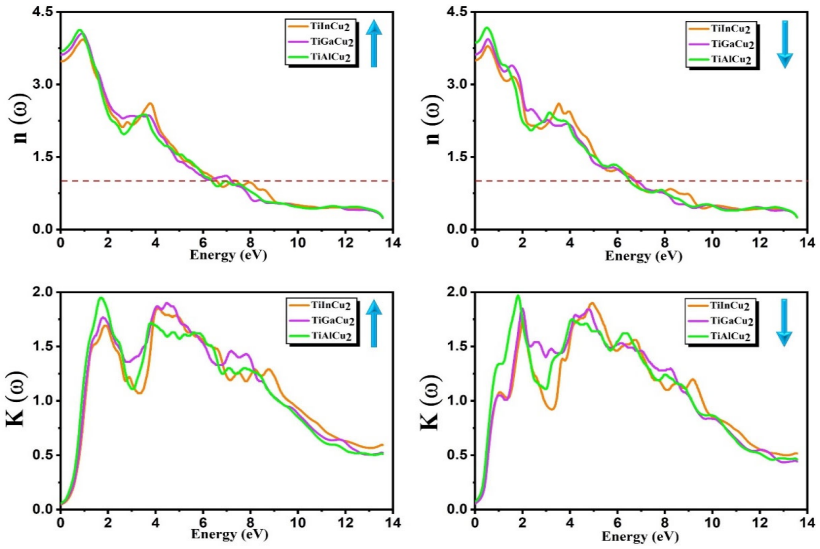


Figure 11. The visual representation of the refractive index $n(\omega)$ and extinction coefficient $K(\omega)$ for $TiMCu_2$ (M = Al, Ga, In).

Based on the results depicted in Figure 11, the initial values of $n(0)$ for $TiMCu_2$ (M = Al, Ga, In) are tabulated in Table 6. The greatest scattering of incident photons in the full-Heusler compounds occurs near 1.0 eV. As shown in Figure 11, $TiMCu_2$ (M = Al, Ga, In) exhibits a largely similar $n(\omega)$ profile, with only slight variations in peak intensity and position. The graphs of $n(\omega)$ cross the y-axis ($n = 1$) at approximately 6.45, 7.23, and 6.66 eV for $TiAlCu_2$, $TiGaCu_2$, and $TiInCu_2$, respectively, in spin $\uparrow$ channel. The plasmon frequency in spin $\downarrow$ channel for $TiAlCu_2$, $TiGaCu_2$, and $TiInCu_2$ are 6.59, 6.68, and 6.82 eV, respectively. This particular point represents the plasmon frequency, where the compounds exhibit metallic characteristics and maintain nearly complete ($\approx 100\%$) photon reflectivity across a wide range of incident light wavelengths.

The extinction coefficient $K(\omega)$, often referred to simply as extinction, characterizes the attenuation of light intensity as a beam propagates through an optical medium. It provides a measure of photon absorption and is closely related to the imaginary part of the dielectric function, $\varepsilon_2(\omega)$. The values of $K(\omega)$ can be obtained from the computed real and imaginary components of the dielectric function, $\varepsilon_1(\omega)$ and $\varepsilon_2(\omega)$, using the following relation:

$$K(\omega) = \left\{ -\frac{\varepsilon_1(\omega)}{2} + \frac{\sqrt{\varepsilon_1^2(\omega) + \varepsilon_2^2(\omega)}}{2} \right\}^{\frac{1}{2}} \tag{11}$$

The $K(\omega)$ spectra for $TiMCu_2$ (M = Al, Ga, In) were computed and are displayed in Figure 11, covering an energy range from 0 to 14.0 eV. The extinction coefficient $K(\omega)$ spectra display distinct peaks, which originate from electronic excitations between the filled states of the valence band (VB) and the unoccupied states of the conduction band (CB). At lower energies, the $K(\omega)$ spectra exhibit no discernible peaks. Following that, the peaks

corresponding to $TiMCu_2$ (M = Al, Ga, In) appear at around 0.0 eV. This value corresponds to the threshold value of $K(\omega)$. The results presented in Figure 11 clearly demonstrate that significant absorption peaks are present in the visible and near UV range. The distinct peaks in the $K(\omega)$ spectra of $TiMCu_2$ (M = Al, Ga, In) are exhibited in the visible region. The energy levels corresponding to the distinct peaks are tabulated in Table 5. Therefore, these full-Heusler compounds exhibit considerable potential for application in solar energy conversion and other optically active devices operating within the visible and near-UV spectral regions.

The optical reflectivity $R(\omega)$ quantifies the proportion of incident photons reflected from the material's surface relative to the total incident flux. Within the framework of linear response theory, $R(\omega)$ can be determined from the complex dielectric function $\varepsilon(\omega)$, as obtained from our electronic structure calculations, through the Fresnel relation:

$$R(\omega) = \left| \frac{\sqrt{\varepsilon(\omega)} - 1}{\sqrt{\varepsilon(\omega)} + 1} \right|^2 = \frac{(1-n)^2 + k^2}{(1+n)^2 + k^2} \tag{12}$$

The $R(\omega)$ spectra for $TiMCu_2$ (M = Al, Ga, In) were computed and are displayed in Figure 12, covering an energy range from 0 to 14.0 eV. The static values, also known as the zero-frequency limit, refer to the values of $R(\omega)$ that are seen at the y-axis when ω is equal to zero. Based on the results depicted in Figure 12, the initial values of $R(0)$ for $TiMCu_2$ (M = Al, Ga, In) are tabulated in Table 6. The highest degree of reflectance of incoming photons in the full-Heusler compounds is $\sim$ 45% in the entire energy span. Figure 12 shows that the reflectivity spectra, $R(\omega)$, of $TiMCu_2$ (M = Al, Ga, In) follow a largely similar trend, with only slight variations in peak intensity and position. The full-Heusler compounds show promise as potential options for anti-reflective coatings.

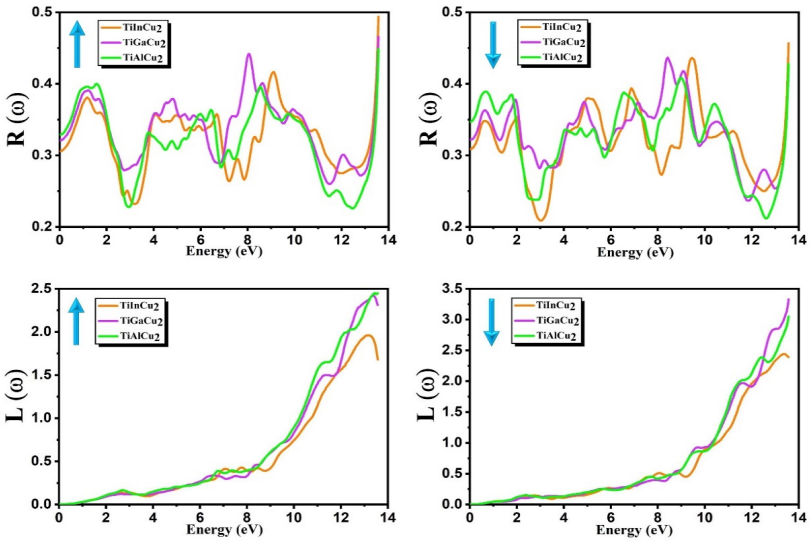


Figure 12. The visual representation of the reflectivity coefficient $R(\omega)$ and energy loss function $L(\omega)$ for $TiMCu_2$ (M = Al, Ga, In).

The likelihood of inelastic electron scattering within the crystal can be evaluated through the energy loss function, $L(\omega)$. This function offers valuable insights into the interaction between electromagnetic radiation and the electronic system and is derived from the computed values of $\varepsilon_1(\omega)$ and $\varepsilon_2(\omega)$.

$$L(\omega) = -ln\left(\frac{1}{\varepsilon}\right) = \frac{\varepsilon_2(\omega)}{\varepsilon_1^2(\omega) + \varepsilon_2^2(\omega)} \tag{13}$$

The $L(\omega)$ spectra for $TiMCu_2$ (M = Al, Ga, In) were computed and are displayed in Figure 12, covering an energy range from 0 to 14.0 eV. The spectra of $L(\omega)$ and $\varepsilon_2(\omega)$ demonstrate precisely opposing patterns. At lower energies, the $L(\omega)$ spectra exhibit no discernible peaks. Following that, the peaks corresponding to $TiAlCu_2$, $TiGaCu_2$, and $TiAlCu_2$ appear at around 0.86, 0.82, and 0.80 eV, respectively. This value corresponds to the threshold value of $L(\omega)$. The distinct peaks in the $L(\omega)$ spectra of $TiMCu_2$ (M = Al, Ga, In) are exhibited in upper UV region. The energy levels corresponding to the distinct peaks are tabulated in Table 5. The full-Heusler compounds display plasmon resonance near the inflection point where the peaks begin to decline from their maximum values.

The real optical conductivity, $\sigma(\omega)$, provides a direct measure of the current density generated through photon absorption in the material. It can be evaluated using the corresponding relation and the calculated values of $\varepsilon_2(\omega)$.

$$\sigma(\omega) = \frac{\omega}{4\pi}\varepsilon_2(\omega) \tag{14}$$

The $\sigma(\omega)$ spectra for $TiMCu_2$ (M = Al, Ga, In) were computed and are displayed in Figure 13, covering an energy range from 0 to 14.0 eV. At lower energies, the $\sigma(\omega)$ spectra exhibit no discernible peaks. Following that, the peaks corresponding to $TiAlCu_2$, $TiGaCu_2$, and $TiAlCu_2$ appear at around 0.51, 0.53, and 0.60 eV, respectively. This value corresponds to the threshold value of $\sigma(\omega)$. The distinct peaks in the $\sigma(\omega)$ spectra of $TiMCu_2$ (M = Al, Ga, In) are exhibited in upper UV region. The energy levels corresponding to the distinct peaks are tabulated in Table 5. Hence, the findings provided in this study indicate that the full-Heusler compounds have considerable promise as viable substitutes for solar cells and other photovoltaic systems operating in the visible and near UV range.

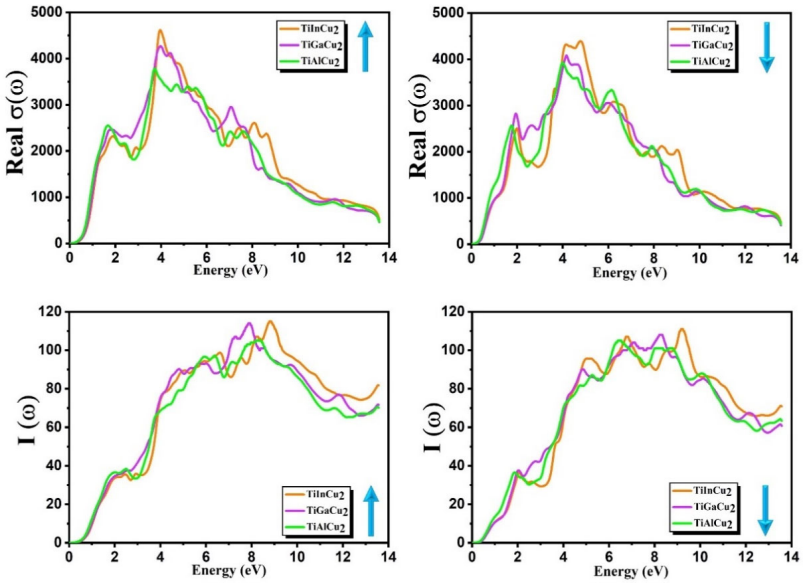


Figure 13. The visual representation of the real optical conductivity $\sigma(\omega)$ and absorption coefficient $I(\omega)$ for $TiMCu_2$ (M = Al, Ga, In).

The penetration depth of photons with energies exceeding the bandgap (E_g) can be evaluated from the absorption coefficient, $I(\omega)$. This coefficient is determined using the derived values of $\varepsilon_1(\omega)$ and $\varepsilon_2(\omega)$ through the corresponding relation.

$$\alpha(\omega) = \sqrt{2\omega}\left\{-\varepsilon_1(\omega) + \sqrt{\varepsilon_1^2(\omega) + \varepsilon_2^2(\omega)}\right\}^{\frac{1}{2}} \tag{15}$$

The $I(\omega)$ spectra for $TiMCu_2$ (M = Al, Ga, In) were computed and are displayed in Figure 13, covering an energy range from 0 to 14.0 eV. At lower energies, the $I(\omega)$ spectra exhibit no discernible peaks. Following that, the peaks corresponding to $TiAlCu_2$, $TiGaCu_2$, and $TiAlCu_2$ appear at around 0.67, 0.71, and 0.78 eV, respectively. This value corresponds to the threshold value of $I(\omega)$. The distinct peaks in the $I(\omega)$ spectra of $TiMCu_2$ (M = Al, Ga, In) are exhibited in upper UV region. The energy levels corresponding to the distinct peaks are tabulated in Table 5. The calculated spectra of $I(\omega)$ for $TiMCu_2$ (M = Al, Ga, In) reveal that photon penetration depth increases with rising photon energy. The $I(\omega)$ spectra confirm that $TiMCu_2$ (M = Al, Ga, In) possess excellent potential for solar and photovoltaic applications in the visible and UV ranges.

3.7. Thermodynamic Properties

The thermodynamic behavior [9] of $TiMCu_2$ (M = Al, Ga, In) is assessed by applying high pressure and temperature through a quasi-harmonic model, executed in Gibbs2 code [60,61]. Temperature has been swept from 0 to 1000 K on three different pressures (0, 5, and 10 GPa). Consequently, we calculated factors such as volume, entropy, Debye temperature, heat capacity, and thermal expansion coefficient. Figure 14 illustrates the thermal expansion coefficient (α) fluctuations for $TiMCu_2$ (M = Al, Ga, In). Till 300 K, α shows an exponential increase with temperature and after that the curves for α show saturation at maximum level. These results show that $TiMCu_2$ (M = Al, Ga, In) absorbs maximum heat at initial temperatures and change in the volume will also be maximum. The specific heat capacities (C_V) of the $TiMCu_2$ (M = Al, Ga, In) are illustrated in Figure 15. At the outset, the specific heat capacity exhibits an increase in the T^3 regime, adhering to the Debye-T^3 law. Subsequently, there is a gradual increase, and at elevated temperatures, it attains the saturation limit, specifically the Dulong Petit limit. Conversely, C_V diminishes gradually with increasing pressure. The plots for entropy (S), representing the level of disorder within the material as pressure and temperature are applied are illustrated in Figure 16. S remains zero at absolute zero, regardless of pressure variations, due to the implications of the third law of thermodynamics. At 0 GPa, the entropy exhibits a significant increase from 0 as the temperature rises. When pressure is applied, there is a decrease in entropy. The application of pressure leads to an increase in the orderliness of the materials, whereas the influence of temperature results in a state of disorder.

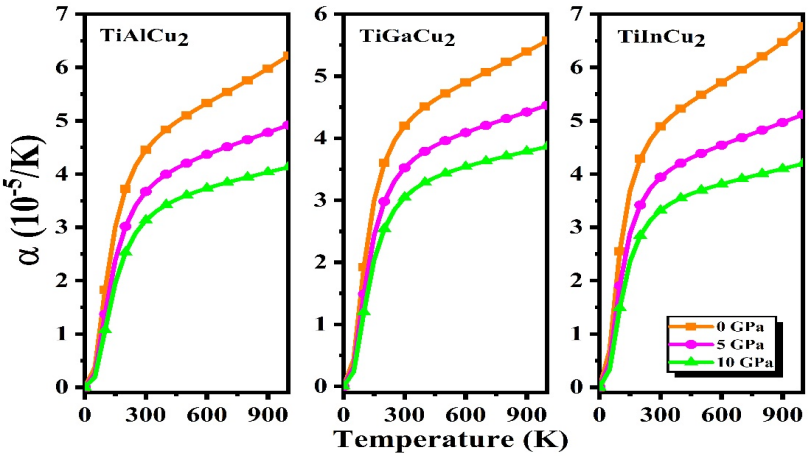


Figure 14. The visual representation of the thermal expansion coefficient (α) for $TiMCu_2$ (M = Al, Ga, In).

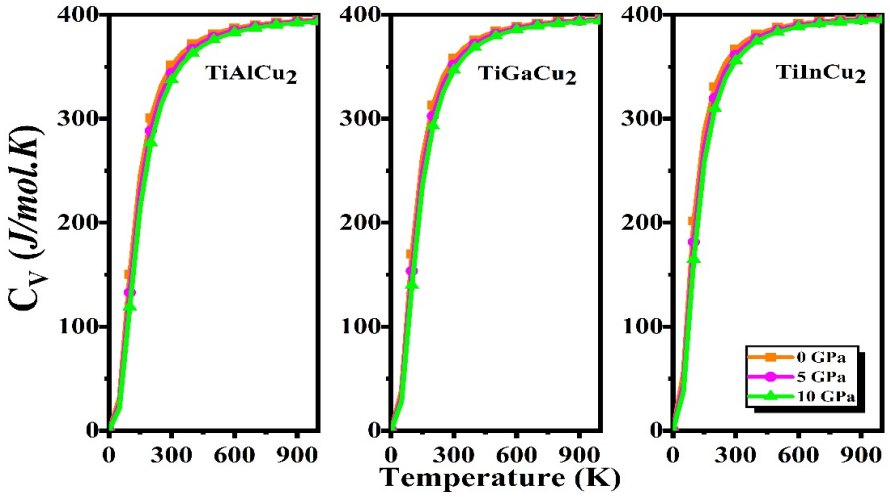


Figure 15. The visual representation of the specific heat capacity at constant volume (C_V) for $TiMCu_2$ (M = Al, Ga, In).

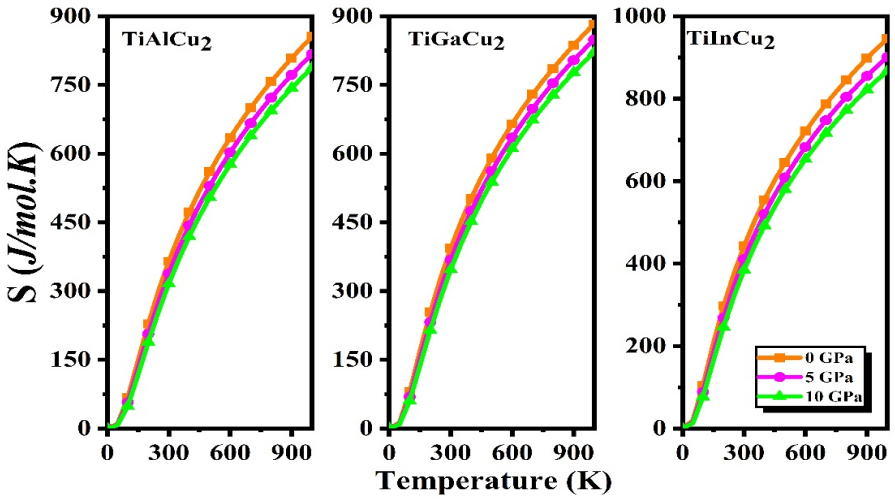


Figure 16. The visual representation of the entropy (S) for $TiMCu_2$ (M = Al, Ga, In).

Additionally, the Debye temperature (Θ_D), which corresponds to three different pressures, is illustrated for $TiMCu_2$ (M = Al, Ga, In) in Figure 17. This parameter is associated with the elastic and mechanical characteristics of solids. The temperature of the crystal is measured at its highest mode of vibration. When the temperature falls below Θ_D, the lattice vibrations of the materials are activated by acoustic vibrations, which cease to exist at temperatures exceeding Θ_D. This parameter is linked to thermal conductivity [62]. Below Θ_D, the atoms in the crystal exhibit restricted movement, suggesting a reduced interaction between electrons and phonons. The solid now operates effectively as a thermal conductor. In Figure 17, a gradual decrease in Θ_D with increasing temperature is noted, while the increase with pressure is significant. Figure 18 illustrates the specific volume (V) fluctuations for $TiMCu_2$ (M = Al, Ga, In). Volume grows gradually with rising temperature at a constant pressure, whereas pressure exerts an inverse impact on volume, resulting in a reduction in volume. This occurs because heat causes material expansion, but pressure induces compression. These calculated thermodynamic characteristics for $TiMCu_2$ (M = Al, Ga, In) show that these compounds are thermally stable compounds.

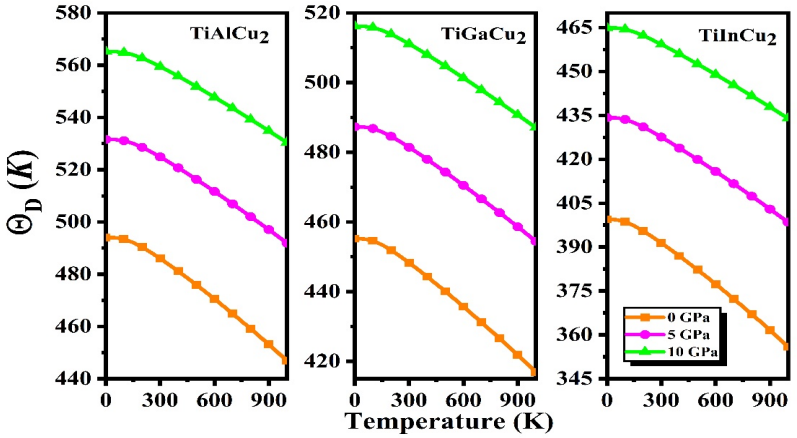


Figure 17. The visual representation of the Debye temperature (Θ_D) for $TiMCu_2$ (M = Al, Ga, In).

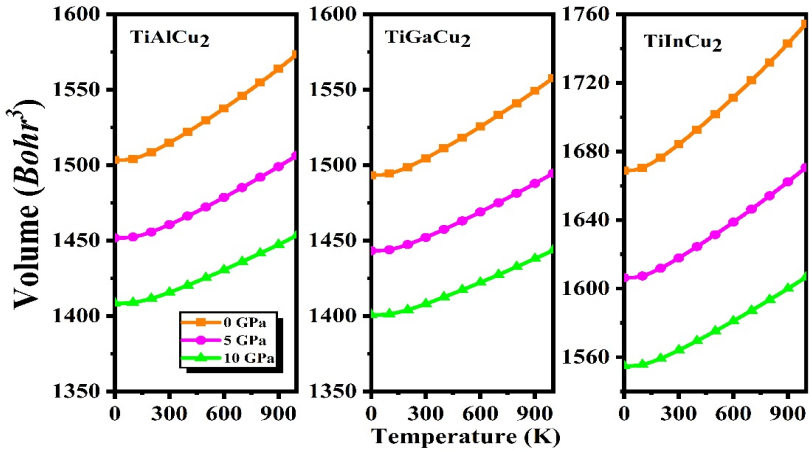


Figure 18. The visual representation of the specific volume (V) for $TiMCu_2$ (M = Al, Ga, In).

4. Conclusions

In this study, the full-Heusler alloys $TiMCu_2$ (M = Al, Ga, In) were systematically explored through GGA+U-based density functional theory. The compounds were found to be structurally and dynamically stable, as confirmed by optimization studies and phonon dispersion analysis. Electronic structure calculations revealed metallic behavior across all systems, with $TiGaCu_2$ exhibiting the highest magnetic moment, making it particularly attractive for spintronic device integration. Optical investigations demonstrated broad absorption in the visible to near-UV range, low reflectivity, and favorable dielectric responses, suggesting strong potential in solar cell and optoelectronic applications. Thermodynamic assessments under varying temperatures and pressures highlighted their robustness and stability, further strengthening their technological relevance. Taken together, these results establish $TiMCu_2$ alloys as multifunctional materials that combine eco-friendly composition, spin polarization, and favorable optical and thermal characteristics. Their unique property portfolio positions them as promising candidates for next-generation spintronic, optoelectronic, and renewable energy technologies.

Author Contributions: Conceptualization, methodology, formal analysis, Z.A.; writing—original draft preparation, investigation A.P., M.T.K.; resources, writing—review and editing, funding acquisition H.I.E., N.M.S. All authors have read and agreed to the published version of the manuscript.

Funding: King Khalid University funded this work through Large Research Project under grant number RGP2/86/46.

Data Availability Statement: All data produced is included in this article.

Acknowledgments: The authors extend their appreciation to the Deanship of Research and Graduate Studies at King Khalid University for funding this work through Large Research Project under grant number RGP2/86/46.

Conflicts of Interest: The authors declare no conflicts of interest.

References

1. Tindibale, E.; Mulwa, W.M.; Adetunji, B.I. Elastic, anisotropic, lattice dynamics and electronic properties of XNiM and XNi2M (X= Ti, Zr, Hf; M= Sn, Ge, Si): DFT comparison study. *Phys. B Condens. Matter.* **2023**, *665*, 415029. [CrossRef]
2. Wang, Y.; Wang, J.; Cai, R.; Zhang, J.; Xia, S.; Li, Z.; Yu, C.; Wu, J.; Wang, P.; Wu, Y. Enhanced Local CO Coverage on Cu Quantum Dots for Boosting Electrocatalytic CO_2 Reduction to Ethylene. *Adv. Funct. Mater.* **2025**, *35*, 2417764. [CrossRef]
3. Zhang, K.; Zhu, C.; Xie, L.; Zhang, L.; Chai, X.; Wu, C.; Wang, S.; Peng, W.; Du, G.; Xu, K. Facile fabrication of electrospun hybrid nanofibers integrated cellulose, chitosan with ZIF-8 for efficient remediation of copper ions. *Carbohydr. Polym.* **2025**, *359*, 123574. [CrossRef] [PubMed]
4. Luo, R.; Zhang, K.; Qin, Y.; Xie, L.; Chai, X.; Zhang, L.; Du, G.; Ge, S.; Rezakazemi, M.; Aminabhavi, T.M.; et al. Amine-functionalized UiO-66 incorporated electrospun cellulose/chitosan porous nanofibrous membranes for removing copper ions. *Chem. Eng. J.* **2024**, *480*, 148077. [CrossRef]
5. Xu, K.; Li, Q.; Xie, L.; Shi, Z.; Su, G.; Harper, D.; Tang, Z.; Zhou, J.; Du, G.; Wang, S. Novel flexible, strong, thermal-stable, and high-barrier switchgrass-based lignin-containing cellulose nanofibrils/chitosan biocomposites for food packaging. *Ind. Crops Prod.* **2022**, *179*, 114661. [CrossRef]
6. Amudhavalli, A.; Dharmaraj, P.; Manikandan, M.; RajeswaraPalanichamy, R.; Iyakutti, K. Investigation of optical properties of Zr2CoZ (Z= Al, Ga, In) full Heusler alloys. *Solid State Sci.* **2023**, *144*, 107307. [CrossRef]
7. Yu, L.; Lei, Y.; Ma, Y.; Liu, M.; Zheng, J.; Dan, D.; Gao, P. A comprehensive review of fluorescence correlation spectroscopy. *Front. Phys.* **2021**, *9*, 644450. [CrossRef]
8. Ren, H.; Xia, X.; Sun, Y.; Zhai, Y.; Zhang, Z.; Wu, J.; Li, J.; Liu, M. Electrolyte engineering for the mass exfoliation of graphene oxide across wide oxidation degrees. *J. Mater. Chem. A* **2024**, *12*, 23416–23424. [CrossRef]
9. Fan, J.; Zhang, X.; He, N.; Song, F.; Zhang, X. Physical absorption and thermodynamic modeling of CO_2 in new deep eutectic solvents. *J. Mol. Liq.* **2024**, *402*, 124752. [CrossRef]
10. Buschow, K.; Van Engen, P. Magnetic and magneto-optical properties of Heusler alloys based on aluminium and gallium. *J. Magn. Magn. Mater.* **1981**, *25*, 90–96. [CrossRef]
11. Kimura, Y.; Tamura, Y.; Kita, T. Thermoelectric properties of directionally solidified half-Heusler compound NbCoSn alloys. *Appl. Phys. Lett.* **2008**, *92*, 012105. [CrossRef]
12. Rai, D.; Sandeep, S.; Shankar, A.; Khenata, R.; Reshak, A.; Ekuma, C.; Thapa, R.; Ke, S.-H. Electronic, optical, and thermoelectric properties of Fe2+ xV1− xAl. *AIP Adv.* **2017**, *7*, 045118. [CrossRef]
13. Winterlik, J.; Fecher, G.H.; Thomas, A.; Felser, C. Superconductivity in palladium-based Heusler compounds. *Phys. Rev. B* **2009**, *79*, 064508. [CrossRef]
14. Liang, S.; Gao, Y.; Hu, C.; Hao, A.; Qin, H. Efficient Photon Beam Diffusion for Directional Subsurface Scattering. *IEEE Trans. Vis. Comput. Graph.* **2024**. [CrossRef]
15. Meng, S.; Meng, F.; Zhang, F.; Li, Q.; Zhang, Y.; Zemouche, A. Observer design method for nonlinear generalized systems with nonlinear algebraic constraints with applications. *Automatica* **2024**, *162*, 111512. [CrossRef]
16. Spataru, C.D.; He, Y.; Léonard, F. Atomistic study of an ideal metal/thermoelectric contact: The full-Heusler/half-Heusler interface. *APL Mater.* **2019**, *7*, 013202. [CrossRef]
17. Poon, S.J. Half Heusler compounds: Promising materials for mid-to-high temperature thermoelectric conversion. *J. Phys. D Appl. Phys.* **2019**, *52*, 493001. [CrossRef]
18. Luo, Y.; Dong, Y. Strain Measurement at up to 3000° C Based on Ultraviolet-Digital Image Correlation. *NDT E Int.* **2024**, *146*, 103155. [CrossRef]
19. Bachagha, T.; Suñol, J.-J. All-d-metal Heusler alloys: A review. *Metals* **2023**, *13*, 111. [CrossRef]
20. Zhang, X.; Chen, H.; Wang, Y.; Gao, X.; Wang, Z.; Wang, N.; Zang, D. Ultrasound induced grain refinement of crystallization in evaporative saline droplets. *Ultrason. Sonochemistry* **2024**, *107*, 106938. [CrossRef]
21. Abbas, Z.; Fatima, K.; Butt, K.; Butt, F.; Hussain, S.; Muhammad, S. Structural, electronic, optical, magnetic and thermodynamics properties of novel half-heusler alloys XNiSb (X= Er, Ho, Yb): First-principles calculations. *Opt. Quantum Electron.* **2023**, *55*, 1070. [CrossRef]
22. Zhang, Y.; Zhuang, X. Cracking elements method for dynamic brittle fracture. *Theor. Appl. Fract. Mech.* **2019**, *102*, 1–9. [CrossRef]
23. Meng, S.; Meng, F.; Chi, H.; Chen, H.; Pang, A. A robust observer based on the nonlinear descriptor systems application to estimate the state of charge of lithium-ion batteries. *J. Frankl. Inst.* **2023**, *360*, 11397–11413. [CrossRef]

24. Chen, S.; Sun, Y.; Zhang, H.; Xu, T.; Zhang, Z.; Han, Q.; Liu, T.; Zou, Y.; Cheng, Z. Mid-Infrared Hyperuniform Disordered Solids Waveguide Devices with Morphology Engineering and Wall-Network Regulation. *Laser Photonics Rev.* **2025**, *19*, 2400469. [CrossRef]
25. Zhang, L.; Wang, X.; Rozale, H.; Lu, J.-W.; Wang, L.-Y. Half-Metallicity and Tetragonal Deformation of Ti 2 RhAl, Ti 2 RhGa, and Ti 2 RhIn: A first-principle study. *J. Supercond. Nov. Magn.* **2016**, *29*, 349–356. [CrossRef]
26. De Groot, R.A.; Mueller, F.M.; van Engen, P.v.; Buschow, K. New class of materials: Half-metallic ferromagnets. *Phys. Rev. Lett.* **1983**, *50*, 2024. [CrossRef]
27. Wang, Y.; Xiao, R.; Xiao, N.; Wang, Z.; Chen, L.; Wen, Y.; Li, P. Wireless multiferroic memristor with coupled giant impedance and artificial synapse application. *Adv. Electron. Mater.* **2022**, *8*, 2200370. [CrossRef]
28. Fang, Q.-L.; Zhang, J.-M.; Xu, K.-W. Magnetic properties and origin of the half-metallicity of Ti2MnZ (Z= Al, Ga, In, Si, Ge, Sn) Heusler alloys with the Hg2CuTi-type structure. *J. Magn. Magn. Mater.* **2014**, *349*, 104–108. [CrossRef]
29. Wang, G.; Feng, W. On-chip Mach-Zehnder interferometer sensor with a double-slot hybrid plasmonic waveguide for high-sensitivity hydrogen detection. *Opt. Express* **2023**, *31*, 39500–39513. [CrossRef]
30. Li, Y.; Liu, G.; Wang, X.; Liu, E.; Xi, X.; Wang, W.; Wu, G.; Wang, L.; Dai, X. First-principles study on electronic structure, magnetism and half-metallicity of the NbCoCrAl and NbRhCrAl compounds. *Results Phys.* **2017**, *7*, 2248–2254. [CrossRef]
31. Doumi, B.; Mokaddem, A.; Sayede, A.; Dahmane, F.; Mogulkoc, Y.; Tadjer, A. First-principles investigations on ferromagnetic behaviour of Be1− xVxZ (Z= S, Se and Te)(x= 0.25). *Superlattices Microstruct.* **2015**, *88*, 139–149. [CrossRef]
32. Han, Y.; Khenata, R.; Li, T.; Wang, L.; Wang, X. Search for a new member of parabolic-like spin-gapless semiconductors: The case of diamond-like quaternary compound CuMn2InSe4. *Results Phys.* **2018**, *10*, 301–303. [CrossRef]
33. Dahmane, F.; Benalia, S.; Djoudi, L.; Tadjer, A.; Khenata, R.; Doumi, B.; Aourag, H. First-principles study of structural, electronic, magnetic and half-metallic properties of the Heusler alloys Ti 2 ZAl (Z= Co, Fe, Mn). *J. Supercond. Nov. Magn.* **2015**, *28*, 3099–3104. [CrossRef]
34. Dahmane, F.; Doumi, B.; Mogulkoc, Y.; Tadjer, A.; Prakash, D.; Verma, K.; Varshney, D.; Ghebouli, M.; Omran, S.B.; Khenata, R. Investigations of the structural, electronic, magnetic, and half-metallic behavior of Co 2 MnZ (Z= Al, Ge, Si, Ga) Full-Heusler compounds. *J. Supercond. Nov. Magn.* **2016**, *29*, 809–817. [CrossRef]
35. Haque, E.; Hossain, M.A. First-principles study of elastic, electronic, thermodynamic, and thermoelectric transport properties of TaCoSn. *Results Phys.* **2018**, *10*, 458–465. [CrossRef]
36. Han, Y.; Chen, Z.; Kuang, M.; Liu, Z.; Wang, X.; Wang, X. 171 Scandium-based full Heusler compounds: A comprehensive study of competition between XA and L21 atomic ordering. *Results Phys.* **2019**, *12*, 435–446. [CrossRef]
37. Han, Y.; Wu, M.; Kuang, M.; Yang, T.; Chen, X.; Wang, X. All-d-metal equiatomic quaternary Heusler hypothetical alloys ZnCdTMn (T= Fe, Ru, Os, Rh, Ir, Ni, Pd, Pt): A first-principle investigation of electronic structures, magnetism, and possible martensitic transformations. *Results Phys.* **2018**, *11*, 1134–1141. [CrossRef]
38. Dahmane, F.; Mesri, D.; Tadjer, A.; Khenata, R.; Benalia, S.; Djoudi, L.; Doumi, B.; Boumia, L.; Aourag, H. Electronic structure, magnetism and stability of Co2CrX (X= Al, Ga, In) ab initio study. *Mod. Phys. Lett. B* **2016**, *30*, 1550265. [CrossRef]
39. Anjami, A.; Boochani, A.; Elahi, S.M.; Akbari, H. Ab-initio study of mechanical, half-metallic and optical properties of Mn2ZrX (X= Ge, Si) compounds. *Results Phys.* **2017**, *7*, 3522–3529. [CrossRef]
40. Yousuf, S.; Gupta, D.C. Investigation of electronic, magnetic and thermoelectric properties of Zr2NiZ (Z= Al, Ga) ferromagnets. *Mater. Chem. Phys.* **2017**, *192*, 33–40. [CrossRef]
41. Wang, X.; Cui, Y.; Liu, X.; Liu, G. Electronic structures and magnetism in the Li2AgSb-type Heusler alloys, Zr2CoZ (Z= Al, Ga, In, Si, Ge, Sn, Pb, Sb): A first-principles study. *J. Magn. Magn. Mater.* **2015**, *394*, 50–59. [CrossRef]
42. Yan, P.-L.; Zhang, J.-M.; Xu, K.-W. Electronic structures, magnetic properties and half-metallicity in Heusler alloys Zr2CoZ (Z= Al, Ga, In, Sn). *J. Magn. Magn. Mater.* **2015**, *391*, 43–48. [CrossRef]
43. Yousuf, S.; Gupta, D.C. Chemical stability and thermodynamics of new Zr_2-based heusler alloys. *Mater. Eng. Res.* **2019**, *1*, 1–6. [CrossRef]
44. Meng, F.; Hao, H.; Ma, Y.; Guo, X.; Luo, H. Site preference of Zr in Heusler alloys Zr2YAl (Y= Cr, Mn, Fe, Co, Ni) and its influence on the electronic properties. *J. Alloys Compd.* **2017**, *695*, 2995–3001. [CrossRef]
45. Khaliq, A.; Zhou, X.; Chai, H.; Ali, M.; Wu, H.; Gassab, O.; Liu, H.; Xiao, D.; Yang, X.-G.; Du, S. Illumination Induced Negative Differential Resistance in InGaAs Avalanche Photodiode. *IEEE Access* **2024**, *12*, 50595–50604. [CrossRef]
46. Heusler, F.; Starck, W.; Haupt, E. Magnetisch-chemische studien. *Verh. Dtsch. Phys. Ges* **1903**, *5*, 219–232.
47. Chen, Y.; Li, C.; Yang, X. Simultaneous measurement of trace dimethyl methyl phosphate and temperature using all fiber Michaelson interferometer cascaded FBG. *Opt. Express* **2023**, *31*, 6203–6216. [CrossRef]
48. Seema, K.; Umran, N.; Kumar, R. Effect of Disorder on Electronic, Magnetic, and Optical Properties of Co 2 CrZ Heusler Alloys (Z= Al, Ga, Si, Ge). *J. Supercond. Nov. Magn.* **2016**, *29*, 401–408.
49. Zhou, H.; Guo, J.; Zhu, G.; Xie, F.; Tang, X.; Luo, X. Highly efficient preparation of crystalline yttrium carbonate in sodium carbonate system: Formation and growth mechanism. *J. Rare Earths* **2025**, *43*, 1492–1501. [CrossRef]

50. Long, Q.; Yan, H.; Wu, H.; Qiu, S.; Zhou, X.; Qiu, T. Influence mechanism of leaching agent anions on the leaching of aluminium impurities in ionic-type rare earth ores: A DFT simulation combined with experimental verification. *Sep. Purif. Technol.* **2025**, *354*, 128768. [CrossRef]
51. Xiong, J.; Wang, Y.; Wang, H.; Xie, L.; Chai, X.; Zhang, L.; Peng, W.; Wang, S.; Du, G.; Xu, K. Electrospun biomass carbon-based porous nanofibers modified by green-dry cold plasma for gaseous formaldehyde adsorption. *Ind. Crops Prod.* **2024**, *222*, 119769. [CrossRef]
52. Elkoua, I.A.; Masrour, R. A comparative study of physical and thermoelectrical characteristics of the new full-Heusler alloys Ag2TiGa and Ag2VGa with ab initio calculations. *Int. J. Quantum Chem.* **2024**, *124*, e27307. [CrossRef]
53. Elkoua, I.A.; Masrour, R. DFT and Monte Carlo study of the structural, elastic, electronic, magnetic and magnetocaloric properties of Ni2MnSi full-Heusler alloys. *Mater. Sci. Semicond. Process.* **2025**, *190*, 109266. [CrossRef]
54. Galta, A.E.; Masrour, R. Exploring the theoretical properties of Rh2TbY (Y = Ga, In) Full-Heusler alloys: Structural, Magneto-electronic, Thermodynamic, and thermoelectric Perspectives. *Comput. Theor. Chem.* **2025**, *1244*, 115008. [CrossRef]
55. Abbas, Z.; Naz, A.; Hussain, S.; Muhammad, S.; Algarni, H.; Ali, A.; Jung, J. First-Principles Calculations to Investigate Structural, Electronic, Optical and Magnetic Properties of Pyrochlore Oxides Eu2Tm2O7 (Tm= Hf, Sn, Zr) for Energy Applications. *Inorganics* **2023**, *11*, 193. [CrossRef]
56. Cai, Y.; Lan, J.; Zhang, G.; Zhang, Y.-W. Lattice vibrational modes and phonon thermal conductivity of monolayer MoS 2. *Physical Review B* **2014**, *89*, 035438. [CrossRef]
57. Rauf, S.; Arif, S.; Haneef, M.; Amin, B. The first principle study of magnetic properties of Mn2WSn, Fe2YSn (Y= Ti, V), Co2YSn (Y= Ti, Zr, Hf, V, Mn) and Ni2YSn (Y= Ti, Zr, Hf, V, Mn) heusler alloys. *J. Phys. Chem. Solids* **2015**, *76*, 153–169. [CrossRef]
58. Galanakis, I.; Dederichs, P.; Papanikolaou, N. Slater-Pauling behavior and origin of the half-metallicity of the full-Heusler alloys. *Phys. Rev. B* **2002**, *66*, 174429. [CrossRef]
59. Zhang, J.; Wang, L.; Zhong, A.; Huang, G.; Wu, F.; Li, D.; Teng, M.; Wang, J.; Han, D. Deep red PhOLED from dimeric salophen Platinum (II) complexes. *Dye. Pigment.* **2019**, *162*, 590–598. [CrossRef]
60. Blanco, M.; Francisco, E.; Luana, V. GIBBS: Isothermal-isobaric thermodynamics of solids from energy curves using a quasi-harmonic Debye model. *Comput. Phys. Commun.* **2004**, *158*, 57–72. [CrossRef]
61. Otero-de-la-Roza, A.; Luaña, V. Gibbs2: A new version of the quasi-harmonic model code. I. Robust treatment of the static data. *Comput. Phys. Commun.* **2011**, *182*, 1708–1720. [CrossRef]
62. Kaur, N.; Srivastava, V.; Dar, S.A.; Khenata, R.; Sharma, R. A unified DFT exploration on transport and thermodynamic properties of L21 structure of Rh2XZn (X= Mn, Fe) ferromagnets. *Mater. Sci. Eng. B* **2023**, *287*, 116099. [CrossRef]

Disclaimer/Publisher's Note: The statements, opinions and data contained in all publications are solely those of the individual author(s) and contributor(s) and not of MDPI and/or the editor(s). MDPI and/or the editor(s) disclaim responsibility for any injury to people or property resulting from any ideas, methods, instructions or products referred to in the content.